Simulations of laser plasma instabilities using a particle-mesh method

H. H. Ma[1,2], C. F. Wu[1,2], S. M. Weng[1,2],* S. H. Yew[1,2], Z. Liu[1,2],
X. F. Li[1,2,3], S. Kawata[4], Z. M. Sheng[1,2,5,6], and J. Zhang[1,2]
[1] *Key Laboratory for Laser Plasmas (MoE), School of Physics and Astronomy,*
Shanghai Jiao Tong University, Shanghai 200240, China
[2] *Collaborative Innovation Center of IFSA, Shanghai Jiao Tong University, Shanghai 200240, China*
[3] *Institute for Advanced Simulation,Jülich Supercomputing Centre,*
Forschungszentrum Jülich, 52425 Jülich, Germany
[4] *Graduate School of Engineering, Utsunomiya University, Yohtoh 7-1-2, Utsunomiya, 321-8585, Japan*
[5] *SUPA, Department of Physics, University of Strathclyde, Glasgow G4 0NG, UK and*
[6] *Tsung-Dao Lee Institute, Shanghai Jiao Tong University, Shanghai 200240, China*

(Dated: June 10, 2021)

A physical model is presented for the study of parametric instabilities in inertial confinement fusion (ICF), which considers the coupling of the incident and scattered electromagnetic waves with plasma electrons and ions. Specially, this model is solved numerically with the particle-mesh method, where the plasma is represented by macro-particles both for electrons and ions, and the velocity and position of each macro-particle are numerically updated by using the particle-mesh method. The developed particle-mesh code in one-dimensional geometry (PM1D) is utilized to study the development of parametric instabilities at the nonlinear stages, where electron plasma wave breaking, particle trapping, hot electron generation and density cavity formation can occur. Particle-in-cell (PIC) simulations are carried out to verify this PM1D code. By comparison, it is found that this PM1D code is able to capture the kinetic effects and precisely describe the developments of parametric instabilities at nonlinear stages as the PIC simulations while saving the computation time obviously. Furthermore, a test simulation of the stimulated Raman scattering evolution up to 200 ps verifies the robustness of this PM1D code.

PACS numbers: 52.38.Kd, 41.75.Jv, 52.27.Ny, 52.65.Rr

I. INTRODUCTION

In laser-drive inertial confinement fusion (ICF), laser plasma instabilities (LPIs) such as stimulated Raman scattering (SRS) and stimulated Brillouin scattering (SBS) develop inevitably[1, 2]. The SRS and SBS not only scatter significant amounts of incident laser energy away from the fusion target, but also degrade the compression symmetry of the target[3–5]. In addition, the SRS can further produce hot electrons due to the wave breaking or the Landau damping of the electron plasma waves (EPWs), which will preheat the DT fuel and decrease the compressibility of the capsule[6–10]. In the direct drive ICF, the SRS can induce the density cavities at around the quarter critical density, which is found to play an important role in the energy absorption of driving lasers[11–13]. In general, the SRS and SBS have significant impacts on the energy deposition of the driving lasers into the capsule and have become one of the biggest obstacles for the realization of ignition in both the direct and indirect laser-drive ICF. Therefore, the evaluation of the impacts of LPIs on the ICF is crucial for the implementation and interpretation of ICF related experiments[14–18].

The numerical simulations can help to deepen the understanding of LPIs and evaluate the impacts of LPIs on the ICF, and thus they have received great attentions in the past decades[19]. At present, the widely used numerical tools for studying laser-plasma interactions can be divided into two kinds: kinetic simulations and fluid simulations[20]. To describe non-equilibrium processes, the kinetic simulations such as particle-in-cell (PIC), Vlasov, and Fokker-Planck simulations solve the particle dynamics in the phase space[21–26]. Therefore, they are competent for the study of various nonlinear phenomena and kinetic effects in the LPI development such as plasma wave breaking[27, 28], particle trapping[29, 30], Landau damping[31, 32], harmonic generation and coupling of different LPI modes [33–35]. Because of their huge computational costs, however, the kinetic simulations are not suitable for the long-time simulations of LPIs in large-scale plasmas[36].

In contrast, fluid simulations solve mass, momentum and energy conservation equations by assuming that the particles satisfy the equilibrium Maxwellian distributions. Generally, fluid simulations cost much smaller computational time than kinetic simulations. Therefore the fluid simulations are more suitable for the macroscopic long-time simulations of LPI. For example, the fluids codes PARAX[36], HERA[37], PF3D[38], LAP3D[39] and so on are developed for the large-scale LPI simulations. In these codes, the paraxial (envelope) approximation is adopted in the wave equations of the electromagnetic waves and the plasma waves in the corresponding three-wave coupling models. The paraxial (envelope) approximation makes it possible to employ a large space

---

* wengsuming@sjtu.edu.cn

and time steps (several times larger than the laser wavelength and cycle) in the simulations, and thus the computational cost greatly decreases. Another kind of fluid codes for the large scale simulations of LPI is based on the 'harmonic decomposition' method. The representative code is HARMONY1D/2D developed by Hüller et al [40], which agrees well with the experiments in the study of the SBS [41]. Recently, the fluid codes LPSE [42, 43] and FLAME [44] are developed for the simulations of cross beam energy transfer (CBET) and the interplay of SRS and SBS in large scales. Since these two fluid codes haven't adopted the paraxial approximation, they are able to capture more nonlinear phenomena of LPI than the fluid codes based on the paraxial approximation. Due to the intrinsic shortage of the fluid model, however, these fluid codes are hard to self-consistently capture the kinetic effects such as wave breaking [27, 28], particle trapping [29, 30], hot electron generation, and Landau damping [31, 32] as well as some nonlinear phenomena such as the formation of density cavity [11–13] in the development of LPIs.

Therefore, it is of great significance to develop a physical model that is competent to simulate macroscopic long-time LPIs and to describe most of kinetic effects and nonlinear phenomena in LPIs simultaneously. In this paper, we present a theoretical model and a numerical method to study the SRS and SBS, where the plasma is described with electron and ion macro-particles. The motions of all macro-particles are governed by the electron and ion momentum equations, and the velocity and position of each macro-particle are numerically updated by using the particle-mesh method. A particle-mesh code in one dimension (PM1D) is then developed, which is able to capture the kinetic effects and save the calculation time simultaneously. The paper is organized as follows: In Sec. II, the fluid model for the development of the SRS and SBS is retrospected. The particle-mesh method for the study of the SRS and SBS is described in Sec. III, in which the plasma is represented by a large number of macro-particles. The motions of macro-particles are governed by the momentum equations and are numerically updated by using the particle-mesh method. The benchmark of the developed PM1D code by using particle-mesh method is presented in Sec. IV. The reproduction of the wave breaking and harmonic generation by the PM1D simulations is illustrated in Sec. V, the simulation of particle trapping is shown in Sec. VI, and the formation of density cavities is illustrated in Sec. VII. The study of convergency and stability of the PM1D code is shown in Sec. VIII. Finally, Sec. IX summarizes the main results with a discussion.

II. FLUID MODEL

In this section, the fluid model for both the SRS and SBS is introduced and summarized. We firstly start from the wave equation that governs the propagating of a laser beam in plasmas[1],

$$(\frac{\partial^2}{\partial t^2} - \nabla^2)a = -4\pi^2 n_e a, \tag{1}$$

where $a = e\boldsymbol{A}/(m_e c^2)$ is the normalized vector potential, here $\boldsymbol{A}$ is the vector potential, m_e is the mass of electron, e is the electron charge and c is the speed of light in a vacuum. In Eq. (1), n_e is the plasma electron density that is normalized to $n_c = \omega_0^2 m_e/(4\pi e^2)$, where ω_0 is the frequency of the incident laser light. The time and space in Eq. (1) are normalized to $2\pi/\omega_0$ and $2\pi c/\omega_0$, respectively. It should be pointed out that the incident and scattered laser lights are described together in a single wave equation in this physical model, i.e., the laser intensity a in Eq. (1) is a superimposed field of the incident laser intensity a_0 and scattered laser intensity a_1 ($a = a_0 + a_1$). By doing so, one does not need to separate the density components of the EPWs or ion acoustic waves (IAWs) from the background electron density. This is distinct from conventional three-wave parametric models, where the separated density components of the plasma waves are coupled with the incident (scattered) laser light to act as the source term in the wave equation for the scattered (incident) laser light[1]. However, when the background electron density or temperature is initially inhomogeneous, the plasma thermal pressure will also induce a density variation and then make it rather difficult to identify the density components of EPWs or IAWs. In contrast, if the incident and the scattered laser lights are described together in a single wave equation, the effects of the density variations due to the plasma thermal pressure and the stimulated plasma waves on the laser propagation can be treated together self-consistently as long as the total electron density is solved. However, this will lead to a numerical difficulty by describing the incident and scattered laser lights together in a single wave equation, i.e. the left boundary condition of the wave equation should allow the pump laser light to enter and the backscattered laser light to exit freely simultaneously. The numerical scheme for solving this boundary issue will be discussed in detail in the next section.

As shown in Eq. (1), the propagating of the laser light in a plasma mainly depends on the time evolution of the total electron density, which can be obtained by solving the fluid equations for the electrons. The dimensionless momentum equation of electrons is [1]

$$\frac{\partial \mathbf{u}_e}{\partial t} + \frac{1}{2}\nabla(\mathbf{u}_e \cdot \mathbf{u}_e) = 4\pi^2\mathbf{E} - \frac{1}{2}\nabla(a \cdot a) - \frac{3v_{eth}^2}{n_e}\nabla n_e, \tag{2}$$

where the electron drift velocity $\mathbf{u}_e$ and electron thermal velocity v_{eth} are normalized to c, the electrostatic field $\mathbf{E}$ induced by the charge separation is normalized to $2\pi c\omega_0 m_e/e$. In Eq. (2), the term $\frac{1}{2}\nabla(a \cdot a)$ is the complete ponderomotive force that includes the contributions not only from the beat wave of the incident and scattered laser lights, but also the uneven envelope of the incident laser beam. Therefore, Eq. (2) can be used for the calculation of the typical LPI processes as well as the density cavity formation induced by electromagnetic soliton around the quarter-critical density in an inhomogeneous plasma[11]. In Eq. (2), the thermal pressure term $\frac{3v_{eth}^2}{n_e}\nabla n_e$ is included to evaluate the temperature effects on LPIs. The dimensionless continuity equation for the electrons is [1]

$$\frac{\partial n_e}{\partial t} + \nabla \cdot (\mathbf{u}_e n_e) = 0. \tag{3}$$

Equations. (2) and (3) serve as the nonlinear fluid equations for the electrons.

To include the SBS into the physical model, the time evolution of the ion density should be solved as well. The dimensionless momentum equation of the ions is

$$\frac{\partial \mathbf{u}_i}{\partial t} + \frac{1}{2}\nabla(\mathbf{u}_i \cdot \mathbf{u}_i) = -4\pi^2 \frac{m_e}{m_i}\mathbf{E} - \frac{v_{ith}^2}{n_i}\nabla n_i, \tag{4}$$

where the ion drift velocity $\mathbf{u}_i$ and the ion thermal velocity v_{ith} are both normalized to c, the ion density n_i is normalized to the critical density n_c, the ion mass m_i is normalized to m_e. In Eq. (4), the electrostatic force $-4\pi^2 \frac{m_e}{m_i}\mathbf{E}$ is the main driving force for the SBS. The ion thermal pressure term $\frac{v_{ith}^2}{n_i}\nabla n_i$ is also included to evaluate the ion temperature effects on the LPIs. The dimensionless continuity equation for the ions can be written as

$$\frac{\partial n_i}{\partial t} + \nabla \cdot (\mathbf{u}_i n_i) = 0, \tag{5}$$

Equation (4) and (5) are the nonlinear fluid equations for the ions, so that the nonlinear evolution of IAWs can be simulated.

In the above model, the precise calculation of the electrostatic field is crucial, since it not only determines the frequency of the EPWs for the SRS development but also transfers the ponderomotive force acting on the electrons to the ions in the SBS development. The dimensionless electrostatic field satisfies the following equation

$$\nabla \cdot \mathbf{E} = n_i - n_e, \tag{6}$$

To sum up, the unified nonlinear fluid model for the SRS and SBS can be written as

$$\begin{cases} (\frac{\partial^2}{\partial t^2} - \nabla^2)a_y = -4\pi^2 n_e a_y, \\ (\frac{\partial^2}{\partial t^2} - \nabla^2)a_z = -4\pi^2 n_e a_z, \\ \frac{\partial n_e}{\partial t} + \nabla \cdot (\mathbf{u}_e n_e) = 0, \\ \frac{\partial \mathbf{u}_e}{\partial t} + \frac{1}{2}\nabla(\mathbf{u}_e \cdot \mathbf{u}_e) = 4\pi^2 \mathbf{E} \\ -\frac{1}{2}\nabla(a_y \cdot a_y) - \frac{1}{2}\nabla(a_z \cdot a_z) - \frac{3v_{eth}^2}{n_e}\nabla n_e, \\ \frac{\partial n_i}{\partial t} + \nabla \cdot (\mathbf{u}_i n_i) = 0, \\ \frac{\partial \mathbf{u}_i}{\partial t} + \frac{1}{2}\nabla(\mathbf{u}_i \cdot \mathbf{u}_i) = -4\pi^2 \frac{m_e}{m_i}\mathbf{E} - \frac{v_{ith}^2}{n_i}\nabla n_i, \\ \nabla \cdot \mathbf{E} = n_i - n_e, \end{cases} \tag{7}$$

where a_y and a_z denote the normalized vector potentials along two vertical directions of y and z, respectively, assuming the propagating direction to be along the x-axis. By doing so, the equation set (7) can be adopted for the study of the laser polarization effects on the LPI.

III. PARTICLE-MESH METHOD

The momentum and continuity equations for the electrons (and ions) in Eq. (7) can be numerically solved on the Eulerian coordinate by the finite difference method directly. However, in the LPI development, the electrons (or ions) will cross each other and induce the breaking of the plasma waves [27, 28, 45]. The wave breaking may cause the saturation of the LPI as well as the production of the hot electrons, and hence it is important to treat the wave breaking properly [9, 10]. However, the wave breaking cannot be described by the finite difference method on the Eulerian coordinate, since the fluid element is not allowed to cross each other in this method. Further, other kinetic effects such as particle trapping in the LPIs cannot be captured by the Eulerian-coordinate-based numerical method as well.

Therefore, we utilize the particle-mesh (PM) method [46] to simulate the plasma dynamics rather than solve the fluid equations of Eq. (7) directly. In the PM method, the simulation box is divided into fixed fluid grids, but the plasma is represented by a large number of macro-particles that are initially distributed uniformly in the grids. Individual macro-particles are driven to move by the fluid force that is defined by the electron or ion momentum equation of Eq. (7). Due to the macro-particles can move freely, the crossing and trapping of macro-particles are allowed. Therefore, it is able to capture the kinetic effects such as particle trapping and hot electron generation. On the other hand, since the macro-particles are driven by the fluid force in the PM method rather than the Lorentz force, the numerical heating in the PM method is relatively weak even with a small number of macro-particles per grid. Therefore, the macro-particle number per grid (cell) used in the PM method can be greatly decreased in comparison with that typically used in the conventional PIC method. As a result, the PM1D code costs much less simulation resources than the conventional PIC codes, while being able to capture the kinetic effects.

A. Numerical algorithm for plasma dynamics

In the PM1D code, the electron and ion macro-particles are initially distributed evenly within the grids with zero velocities, that is

$$\begin{array}{l} v_{sk}^0 = 0, k = 1 \ldots M, s = e, i, \\ x_{sk}^0 = x_{s1}^0 + \frac{dx}{P}(k-1), k = 1 \ldots M, s = e, i, \end{array} \tag{8}$$

where v_{sk}^0 and x_{sk}^0 are the initial velocity and position of the k-th macro-particle, s denotes the particle species of ions or electrons, P and M are the macro-particle numbers for the s-th particle species in each grid and the entire simulation box, respectively. For an initial electron or ion density $n_s^0(x)$, the density fraction for the k-th macro-particle of the s-th species can be written as

$$w_s^k = \frac{n_s^0(x_{sk}^0)}{P}, s = e, i, \tag{9}$$

The density fractions of every maro-particles keep unchanged in the simulation, which guarantees the continuity equation of Eq. (7). The electron or ion density distribution on the grids can be obtained by the interpolation method according to the positions of the macro-particles[47]. The total driving forces are firstly calculated on the grids and then interpolated to macro-particles. Assuming the total driving forces for the electron and ion particles are F_e and F_i, respectively, then we have

$$\begin{aligned} F_e &= 4\pi^2 \mathbf{E} - \tfrac{1}{2}\nabla(a \cdot a) - \tfrac{3v_{eth}^2}{n_e}\nabla n_e, \\ F_i &= -4\pi^2 \tfrac{m_e}{m_i}\mathbf{E} - \tfrac{v_{ith}^2}{n_i}\nabla n_i. \end{aligned} \tag{10}$$

The driving forces of Eq. (10) can be discretized as follows

$$\begin{aligned} F_{ej}^n &= 4\pi^2 E_j^n - a_j^n \tfrac{a_{j+1}^n - a_{j-1}^n}{2dx} - \tfrac{3v_{eth}^2}{n_{ej}^n}\tfrac{n_{ej+1}^n - n_{ej-1}^n}{2dx}, \\ F_{ij}^n &= -4\pi^2 \tfrac{m_e}{m_i} E_j^n - \tfrac{3v_{ith}^2}{n_{ij}^n}\tfrac{n_{ij+1}^n - n_{ij-1}^n}{2dx}, \end{aligned} \tag{11}$$

where F_{ej}^n and F_{ij}^n are the total driving force to the electrons and ions at the j-th point and the n-th time step, respectively.

After the driving forces for the k-th macro-particle of the s-th species at the n-th time step $F_s^n(x_{sk}^n)$ are obtained by the interpolation method, the position and velocity of the k-th macro-particle can then be updated for the $(n+1)$-th time step by the following second order Runge-Kutta method [48], that is

$$\begin{cases} v_{sk}^{n+1/2} = v_{sk}^n + dtF_s^n(x_{sk}^n), \\ x_{sk}^{n+1/2} = x_{sk}^n + \frac{1}{2}dt(v_{sk}^{n+1/2} + v_{sk}^n), \\ v_{sk}^{n+1} = \frac{1}{2}(v_{sk}^{n+1/2} + v_{sk}^n) + \frac{1}{2}dtF_s^{n+1/2}(x_{sk}^{n+1/2}), \\ x_{sk}^{n+1} = x_{sk}^n + \frac{1}{2}dt(v_{sk}^n + v_{sk}^{n+1/2}), s = e, i \end{cases} \tag{12}$$

where x_{sk}^{n+1} and v_{sk}^{n+1} are the position and velocity of the k-th particle at the $(n+1)$-th time step of s species, respectively, while $x_{sk}^{n+1/2}$ and $v_{sk}^{n+1/2}$ are the intermediate variables of position and velocity for the k-th particle, respectively.

B. Numerical algorithm for wave equation

To calculate the vector potential a, the wave equation of Eqs. (7) are discretized by the typical central difference method as [49],

$$\frac{a_j^{n+1} - 2a_j^n + a_j^{n-1}}{dt^2} - \frac{a_{j+1}^n - 2a_j^n + a_{j-1}^n}{dx^2} = -4\pi^2 n_{ej}^n a_j^n, \tag{13}$$

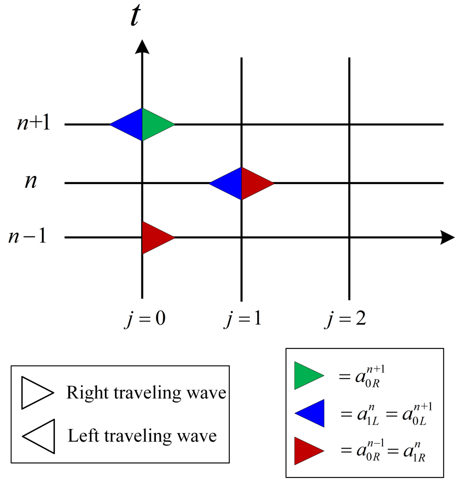

FIG. 1. The schematic diagram for the left boundary condition of the wave equation. The relationships between the right-traveling and left-traveling waves at the points $j = 0$ and $j = 1$ at different time steps of $n-1$, n, and $n+1$ are illustrated.

where dt and dx are respectively the time and space steps, the subscript j and the superscript n respectively denote the j-th grid point in space and the n-th time step. The vector potential a at the $(n+1)$-th time step can be updated according to Eq. (13) as long as the electron density at the n-th time step is already known. To solve the wave equation, the boundary condition for the electromagnetic field is also necessary. As mentioned above, when the incident and scattered laser lights are described together in a single wave equation, the left boundary should allow the incident laser to enter the simulation box and the backscattered laser to exit the simulation box freely. To this end, the simulation box is divided into three parts, including a central plasma slab and two vacuum regions on two sides. In two vacuum regions, the dimensionless speed of the laser light is 1, which makes it convenient to set the boundary condition for the electromagnetic field. For example, we assume that the left boundary is located at the point of $j = 0$ and the vector potential on the boundary at the $(n+1)$-th time step is a_0^{n+1}. For convenience, the vector potential on the boundary at the $(n+1)$-th time step can be divided into two parts as

$$a_0^{n+1} = a_{0R}^{n+1} + a_{0L}^{n+1}, \tag{14}$$

where a_{0R}^{n+1} and a_{0L}^{n+1} are the vector potentials of the right and left traveling waves on the boundary, respectively. In the case of $dx = dt$, the propagating distance of a laser light in a vacuum within a time step is just dx. Thus, the vector potential of the left traveling wave at the point $j = 0$ and the $(n+1)$-th time step is just its value at the point $j = 1$ and the n-th time step as shown in Fig. 1, namely

$$a_{0L}^{n+1} = a_{1L}^{n}. \tag{15}$$

Similarly, the vector potential at the point $j = 1$ and n-th time step can also be divided into the left and right traveling wave components, so we have

$$a_{1L}^{n} = a_{1}^{n} - a_{1R}^{n}, \tag{16}$$

where a_1^n denotes the total vector potential at the point $j = 1$ and the n-th time step, a_{1L}^n and a_{1R}^n are left and right traveling waves components, respectively. As shown in Fig. 1, the right traveling wave component a_{1R}^n is exactly the vector potential of the right traveling wave at the point $j = 0$ and $(n-1)$-th time step, that is

$$a_{1R}^{n} = a_{0R}^{n-1}. \tag{17}$$

Combing Eqs. (14-17), the left boundary condition in the case of $dt = dx$ can be written as

$$a_{0}^{n+1} = a_{0R}^{n+1} + a_{1}^{n} - a_{0R}^{n-1}, \tag{18}$$

where the right traveling wave components a_{0R}^{n+1} and a_{0R}^{n-1} are the incident pump laser light, and the vector potential at the point of $j = 1$ and n-th time step a_1^n is already obtained in the last loop. Similarly to Eq. (18), the left boundary condition in the general case of $dt \neq dx$ can be derived as

$$a_{0}^{n+1} = a_{0R}^{n+1} + \frac{dt}{dx}(a_{1}^{n} - a_{0}^{n}) + a_{0}^{n} - a_{0R}^{n-1}. \tag{19}$$

Similarly, the right boundary can also be set to allow the right traveling waves to be absorbed and the left traveling waves to be input, namely

$$a_{H+1}^{n+1} = a_{(H+1)L}^{n+1} + \frac{dt}{dx}(a_{H}^{n} - a_{H+1}^{n}) + a_{H+1}^{n} - a_{(H+1)L}^{n-1}, \tag{20}$$

where the subscript of $(H + 1)$ is the right boundary point.

C. Program flow

To sum up, the plasma dynamics and the wave equation in the PM1D can be solved as follows:

1. Calculate the vector potential of a at the $(n+1)$-th time step using Eq. (13) combing with the corresponding boundary conditions Eqs. (19) and (20).
2. Calculate the electron and ion density distribution by depositing all macro-particles onto the grids using the interpolation method.
3. Obtain the electrostatic field by solving Eq. (6).
4. Calculate the total forces on the grids using Eq. (11), and interpolate the driving force to every macro-particle.
5. Calculate the velocity and position of all macro-particles at the $(n + \frac{1}{2})$-th time step by Eq. (12).
6. Repeat steps 2 and 4 using the intermediate particle positions to get the newly driving forces acting on the macro-particles.
7. Calculate the velocity and position of all macro-particles at the $(n + 1)$-th time step by Eq. (12).
8. Repeat steps 1-7 until the final time arrives.

D. Differences among PM1D, PIC and fluid codes

In the PM1D code, the plasmas is treated as a gather of macro-particles. The motion of macro-particles is calculated according to the momentum equations in Eq. (7). Actually, the left terms $\frac{\partial \mathbf{u}}{\partial t} + \frac{1}{2}\nabla(\mathbf{u}\cdot\mathbf{u})$ in the momentum equations of Eq. (7) is the total derivative of a particle velocity versus time. Therefore, the right terms of the momentum equations in Eq. (7) are the drive forces for a single macro-particle. In the simulations, these driving forces are firstly calculated on the fixed meshes. Then the total force acting on a macro-particle is obtained by the interpolation method and the particle velocity at the next time step is calculated using Eq. (12).

In the PIC code (e.g. EPOCH code), the velocities of macro-particles are calculated according to the following equation [47]

$$\mathbf{P}_{\alpha}^{n+1} = \mathbf{P}_{\alpha}^{n} + q_{\alpha}\Delta t[\mathbf{E}^{n+1/2} + \mathbf{v}_{\alpha}^{n+1/2} \times \mathbf{B}^{n+1/2}], \tag{21}$$

where q_α is the particle's charge, $\mathbf{P}_\alpha$ is the particle momentum, and $\mathbf{v}_\alpha$ is the particle velocity. Here the particle velocity of $\mathbf{v}_\alpha$ can be calculated using $\mathbf{P}_\alpha = \gamma_\alpha m_\alpha \mathbf{v}_\alpha$, where $\gamma_\alpha = [(\mathbf{P}_\alpha/m_\alpha c)^2 + 1]^{1/2}$ is the relativity factor and m_α is the particle mass. From Eq. (21), one can find that in a typical PIC code the macro-particles are driven to move by the Lorentz force, while in the PM1D code the macro-particles are driven to move by the fluid forces of Eq. (10). This is the main difference between the PIC code and PM1D code.

In the typical wave coupling method [36–39, 42–44], the finite difference methods are adopted to solve the fluid equations directly. In contrast, the PM1D code does not directly solve the fluid equations for the plasma dynamics. Instead, the plasma is represented by a gather of macro-particles in the PM1D code, and the motion of these macro-particles is numerically updated by the particle-mesh method. More importantly, since the electron and ion macro-particles can move freely in the particle-mesh method, various kinetic effects can be self-consistently treated in the PM1D code.

IV. BENCHMARK OF PM1D CODE

To verify the PM1D code, we firstly compare the linear growth rates of both the SRS and SBS obtained from our PM1D simulations with theoretical estimations. For the

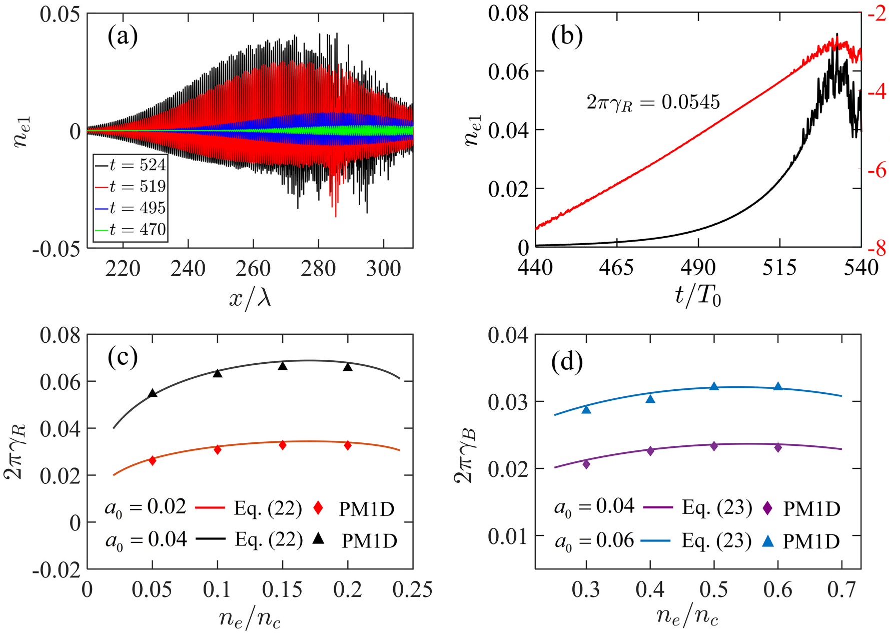

FIG. 2. (a) The snapshots of the chosen wave packet of the EPW at four different times. (b) The black line and red line show the time evolution of the peak amplitude of the chosen wave packet and its logarithm, respectively (c) The linear SRS growth rates ($2\pi\gamma_R$) as a function of the electron density obtained from the PM1D simulations (red points for $a_0 = 0.02$ and black points for $a_0 = 0.04$) are compared with the theoretical results estimated by Eq. (22)(red line for $a_0 = 0.02$ and black line for $a_0 = 0.04$). The initial electron temperature is set as 1 keV and ions are assumed to be immobile. (d) linear SBS growth rates ($2\pi\gamma_B$) as a function of the electron density obtained from the PM1D simulations (the purple points for $a_0 = 0.04$ and the blue points for $a_0 = 0.06$) are compared with the theoretical results estimated by Eq. (23) (the purple line for $a_0 = 0.04$ and the blue line for $a_0 = 0.06$). The initial electron temperature is set as 1 keV and the ions are assumed to be cold initially.

SRS, the theoretical growth rate γ_R in the linear stage can be expressed as [1]

$$\gamma_R = \frac{ka_0}{4}\left[\frac{\omega_{pe}^2}{\omega_{ek}(\omega_0 - \omega_{ek})}\right], \tag{22}$$

where γ_R is normalized to ω_0, a_0 is the normalized vector potential of pump laser light, k is the wave number of the EPW, ω_{pe} is the plasma frequency and $\omega_{ek} = \sqrt{\omega_{pe}^2 + 3k^2 v_{eth}^2}$. The growth rate of the SRS in Eq. (22) is actually defined as the growth rate of the EPW amplitude. So for comparison, the growth rate of the EPW amplitude should be extracted from the PM1D simulation results. As displayed in Fig. 2(a), the strongest packet of the EPW is firstly recognized at different times in a typical PM1D simulation with the normalized laser vector potential $a_0 = 0.04$, the electron density $n_e = 0.05n_c$ and temperature $T_e = 1$ keV (corresponding to the far left black point in Fig. 2(c)). Then, the time evolution of the peak amplitude of the EPW can be obtained as the black curve in Fig. 2(b). If the peak amplitude of the EPW grows exponentially, then the logarithm of the EPW peak amplitude should be a straight line whose slope corresponds to the growth rate of the SRS. In Fig. 2(b), the logarithm of the EPW peak amplitude is drawn as a red line, which has a slope about 0.0545 between $t = 465T_0$ and $515T_0$. The numerical growth rate defined by this slope is coincident with the theoretical result $2\pi\gamma_R = 0.0542$ estimated by Eq. (22). Similarly, the growth rate of the SBS can be estimated as the growth rate of the peak amplitude of an ion acoustic wave packet obtained from the PM1D simulation.

In Fig. 2(c), the SRS growth rates obtained from the PM1D simulations (discrete points) are compared with the theoretical results estimated by Eq. (22) (lines). It can be found that the quantitative agreement in the growth rate is achieved between the PM1D code and the theory, indicating that the PM1D code is competent for the precise calculation of the SRS.

For the SBS, the linear growth rate γ_B can be expressed as [1],

$$\gamma_B = \frac{1}{2\sqrt{2}}\frac{k_0 a_0 \omega_{pi}}{\sqrt{\omega_0 k_0 C_s}}, \tag{23}$$

where γ_B is normalized to ω_0, k_0 and ω_0 are respectively the wave number and frequency of the pump laser light in the plasma. $\omega_{pi} = \omega_{pe}\sqrt{Zm_e/m_i}$ with the ion charge $Z = 1$, and $C_s = \sqrt{ZT_e/m_i}$ is the ion acoustic velocity. As shown in Fig. 2(d), the SBS growth rates calculated by the PM1D code (discrete points) also agree quantitatively with those estimated by Eq. (23) (lines), which demonstrates the capability of the PM1D code in the

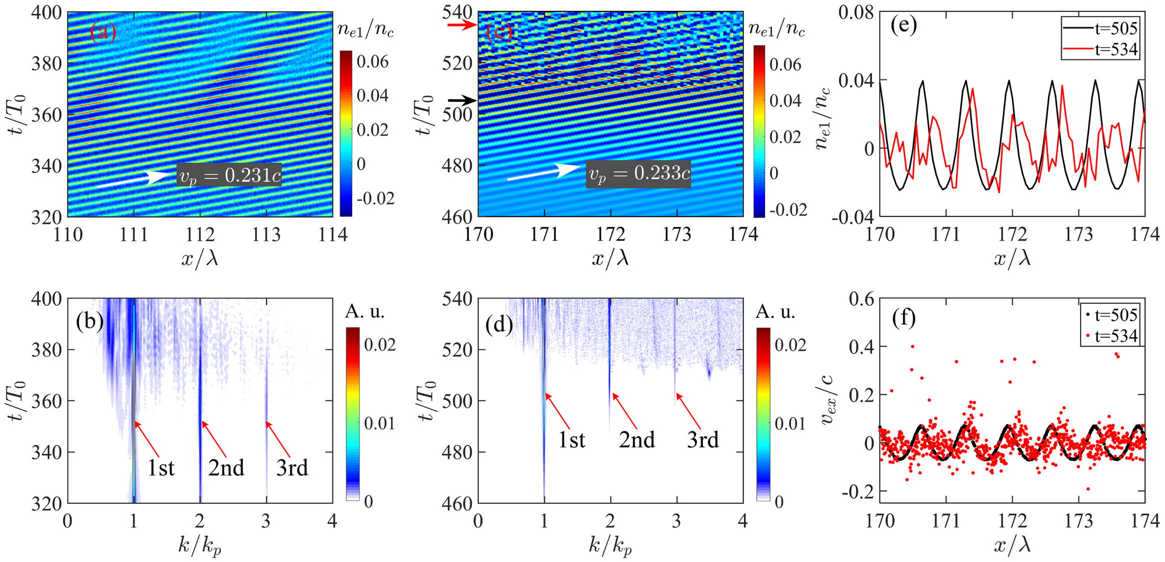

FIG. 3. (a) and (c) show the time evolution of EPWs (where n_{e1} denotes the fluctuating electron density) calculated by PIC code and PM1D code, respectively. The slope of the white arrow in (a) and (c) show the phase speed of EPWs. (b) and (d) shows the time evolution of the wave-number spectrum of the EPWs in (a) and (c), respectively, where k_p is the theoretical wave number of the EPW. The 1st, 2nd and 3rd-order harmonics of the EPWs can be found in the wave-number spectrum. (e) The snapshot of the EPW at the times that are signed by the black ($t = 505T_0$ before the wave breaking) and the red($t = 534T_0$ after the wave breaking) arrows in (c). (f) The $x - v_{ex}$ phase space of the electron macro-particles in (e). The hot electron generation after the wave breaking is illustrated.

precise calculation of the SBS.

V. SIMULATION OF WAVE BREAKING

With the developing of the SRS, the amplitude of the EPW excited by SRS will reach a peak value and then start to decay due to the wave breaking. Along with the saturation of the SRS [28, 45], the wave breaking will also induce the generation of hot electrons [9, 10] and the bursting behavior of the reflectivity of SRS[50]. Therefore, the breaking process of the EPW is crucial for the evolution of the SRS and should be included properly in the physical model. In our PM1D code, the electron and ion fluids are represented by freely moving macro-particles, which can be used to simulate the wave-breaking process. To verify this, a test simulation is carried out, in which the simulation box has a total length of 300λ with a length of 20λ vacuum in each side, here λ is the incident laser wavelength in a vacuum. A hydrogen plasma slab is located within $20\lambda \leq x \leq 280\lambda$, the plasma slab has a length of 10λ density slopes on both sides, and the electron density $n_e = 0.1n_c$ at the flat-top. The initial electron temperature is set as 2 keV and the ions are assumed to be immobile. The incident laser light has an intensity of 1.78×10^{16} W/cm^2 and a wavelength of 351 nm, correspondingly $a_0 = 0.04$. The time and space steps are set as $0.0495T_0$ and 0.05λ, respectively, and 5 macro-particles are allocated for each grid. For comparison, a PIC simulation is carried out using the EPOCH code[47], where the laser and plasma conditions keep the same as adopted in the PM1D simulation. The space step of PIC simulation is $dx = 0.01\lambda$ and 600 macro-particles are set in every grid.

Figure 3(a) shows the time evolution of the EPW within $110\lambda \leq x \leq 114\lambda$ calculated by the PIC code. It can be found that the EPW moves to the right at a nearly constant phase velocity of $v_p \simeq 0.231c$, which agrees well with the theoretical estimate $v_p \simeq 0.236c$. More importantly, the EPW begins to collapse at $t \geq 360T_0$, which implies the occurrence of the wave breaking. Correspondingly, the time evolution of the wave number spectrum of the EPW is shown in Fig. 3(b), in which the 2nd and 3rd order harmonic generations of the EPW are evidenced.

In Fig. 3(c), the time evolution of the EPW within $170\lambda \leq x \leq 174\lambda$ calculated by PM1D code is shown during the development of the backward SRS. It can be found that the EPW moves to the right at a nearly constant phase speed of $v_p \simeq 0.233c$, which agrees well with the theoretical phase speed $0.2358c$. More importantly, the EPW amplitude grows continuously before $t \simeq 510T_0$, then the EPW reaches its peak amplitude and starts to break up. After the wave breaking ($t > 520T_0$), the EPW will become relatively weak, resulting in an obvious decrease of the SRS reflectivity (i.e. the saturation of SRS). After that, new EPW packets may start to form, which will induce a considerable reflectivity again. Namely, the SRS reflectivity varies with the growing and collapsing of the EPW, which results in the bursting behavior of the SRS reflectivity[50] . Correspondingly, the

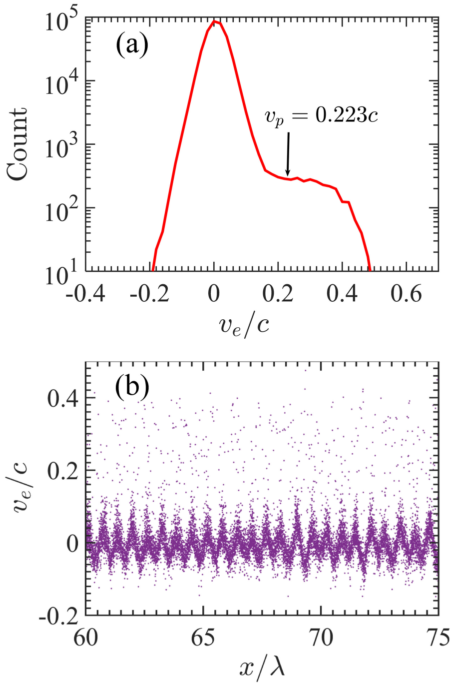

FIG. 4. (a) The velocity distribution of electrons at $1000T_0$. The black arrow shows the phase speed of the EPW. (b) The phase space of electrons within $60\lambda < x < 75\lambda$ at $1000T_0$.

time evolution of the wave-number spectrum of the EPW in Fig. 3(c) is displayed in Fig. 3(d). It is illustrated that the EPW has a single wave number before $t = 490T_0$, and later the 2nd and 3rd order harmonics appear sequentially. The harmonic generation of EPW is a typical nonlinear phenomenon, which can also appear for the IAWs in the SBS [33–35, 51]. The higher-order harmonics of EPW do not satisfy the resonance condition of the SRS and will further induce a frequency shift[52]. Therefore, the harmonic generation of the EPW is one of the saturation mechanisms for the SRS. Further, the wave-number spectrum becomes broader after the wave breaking ($t > 510T_0$), indicating the collapse of the EPW.

From the above comparison, it is found that the time evolution of EPW and its harmonic generation calculated by the PM1D code agree well with those calculated by the PIC code, which further demonstrates the capability of the PM1D code in simulating kinetic effects and nonlinear phenomena in the LPI development. However, it should be pointed out that the harmonic generation as well as the collapse of the EPW happen in an earlier time in the PIC simulation, this might be due to the higher density noise in the PIC simulations.

In Fig. 3(e), we display the snapshots of the EPW at the times that are marked by the black ($t = 505T_0$ before the wave breaking) and red ($t = 534T_0$ after the wave breaking) arrows in Fig. 3(c), respectively. It should be pointed out that the EPW still shows a periodic perturbation at $t = 505T_0$ before the wave breaking, but it is no longer in cosine form due to the harmonic generation. In contrast, the EPW seems more chaotic at $t = 534T_0$ after the wave breaking. Correspondingly, the electron distribution in the $x - v_{ex}$ phase space before and after the wave breaking are compared in Fig. 3(f). It can be found that the electrons are distributed in order in the space with gentle velocities before the wave breaking ($t = 505T_0$). After the wave breaking, the electrons lost their spatial orders and some of the them are accelerated to high velocities ($v_e > 0.4c$). In other words, the hot electrons ($T_e > 100kev$) are generated due to the wave breaking. It should be pointed out that those hot electrons are accelerated efficiently from a relative low velocity of about $0.1c$ to over $0.4c$ within $30T_0$ (35 fs) in the wave breaking process. In addition, Fig. 3(f) indicates that the hot electrons move in the same direction with the EPW.

VI. SIMULATION OF PARTICLE TRAPPING

In the high-temperature plasma conditions relevant to ICF experiments, the particle trapping and Landau damping are the most important kinetic effects in the development of the LPIs. Therefore, a highly reliable LPI simulation tool should include these kinetic effects. The cause of the particle trapping and Landau damping is that the particles with velocities closed to the EPW phase speed will be captured and accelerated (or decelerated) by the electrostatic field of the EPW [1]. Therefore, when driving forces of the electron macro-particles include the electrostatic force (as shown in Eq. (10)) and the macro-particles can move freely, the particle trapping and Landau damping can be treated self-consistently. To verify this, a test simulation is performed, in which the electron density $n_e = 0.09n_c$, the electron temperature $T_e = 1$ keV, the laser intensity $a_0 = 0.02$ and the ions are assumed to be immobile. The plasma has a total length of 400λ, and the space step is $dx = 0.05\lambda$ with 50 macro-particles per grid.

Figure 4(a) shows the velocity distribution of the electrons in the whole simulation domain at $t = 1000T_0$. It is clear that the electron velocity distribution becomes flat at around the phase speed of the EPW, which indicates the obvious particle trapping of the electrons during the SRS evolution [30, 50]. Figure 4(b) shows the phase space of the electrons within $60\lambda < x < 75\lambda$ at $t = 1000T_0$, which clearly demonstrates the hot electron generation as well as the electron trapping. The simulation results in Fig. 4 indicates that the PM1D code is able to capture the kinetic effects such as particle trapping as the PIC codes.

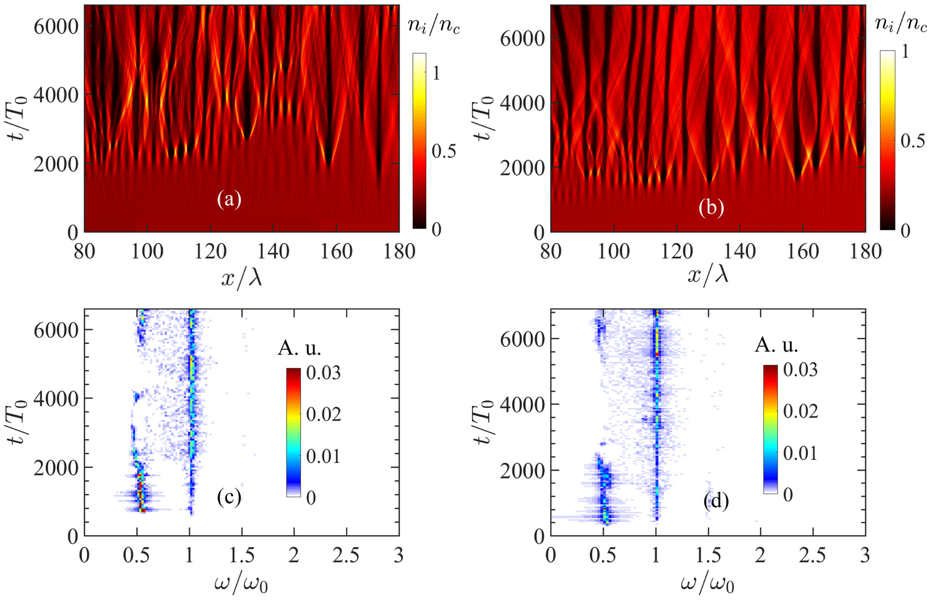

FIG. 5. The time evolutions of the ion densities within $80\lambda \leq x \leq 180\lambda$ during the density cavity formation that are obtained from the PM1D (a) and PIC (b) simulations. The corresponding frequency spectra of the backscattered lights are displayed in (c) and (d), respectively.

VII. SIMULATION OF DENSITY CAVITY FORMATION

In the direct-drive ICF, the SRS at around the quarter-critical density becomes an absolute instability[53], and the scattered laser light has a central frequency of $0.5\omega_0$. According to the dispersion relation, the backscattered laser light will have a zero wave number and can be trapped as an electromagnetic soliton at this position. Due to the continuous energy pumping from the incident laser light, the trapped backscattered laser light is continuously enhanced, whose strong ponderomotive forces will push away the ions to form density cavities[11, 12]. To simulate the formation of the density cavity, the ponderomotive force of a laser beam with an uneven envelope in space should be included in the physical model. In the PM1D code, a complete form of the ponderomotive force is employed, thus it should simulate the density cavity formation properly.

To verify this, a test simulation is carried out. In the simulation, an inhomogeneous plasma slab with a linear density profile ranging from $0.22n_c$ to $0.28n_c$ is adopted, the plasma slab has a length of 220λ with a 10λ up-ramp at the left and a 10λ density down-ramp at the right. The total length of the simulation box is 340λ with a 60λ vacuum in each side. The electron and ion initial temperatures are set as 1keV and 0.1keV, respectively. The incident laser light has an intensity of 1×10^{16} W/cm^2 and a wavelength of 351 nm, the corresponding normalized vector potential $a_0 = 0.03$. The time step was $dt = 0.019T_0$, the grid size $dx = 0.02\lambda$, and 10 macro-particles per grid are used in the PM1D code. For comparison, a PIC simulation is carried out using the EPOCH code[47]. Except that 400 macro-particles per cell are used in the PIC simulation, the spatial and temporal resolutions and laser-plasma parameters are the same as those in the PM1D simulation.

Figures 5(a) and 5(b) compare the time evolutions of the ion densities within $80\lambda \leq x \leq 180\lambda$ (corresponding to background plasma density varies from $0.223n_c - 0.253n_c$) obtained from the PM1D and PIC simulations. It is illustrated that many plasma density cavities emerge after $1500T_0$, and then the ion densities in the cavities gradually decrease to zero. Meanwhile, the widths of the density cavities increase gradually and some cavities may merge with the adjacent cavities. As shown in Figs. 5(a) and 5(b), both the PM1D and PIC simulations can capture the formation of the density cavities, and output similar results.

Figures 5(c) and 5(d) show the time evolutions of the frequency spectra of the backscattered laser lights calculated by the PM1D code and PIC code, respectively. It indicates that the SRS firstly develops for $t < 2500T_0$, but later the SBS becomes dominant and the SRS nearly disappears during $2500T_0 < t < 6000T_0$. More interestingly, both the PM1D and PIC simulations show that the backscattered SRS lights will grow up again after $t = 6000T_0$, because of the collapse of the density cavities.

Along with the formation of the plasma density cavity, many other nonlinear effects could also play an important role in the development of parametric instabilities near the quarter-critical density. For example, it was found that the Langmuir decay instability (LDI),

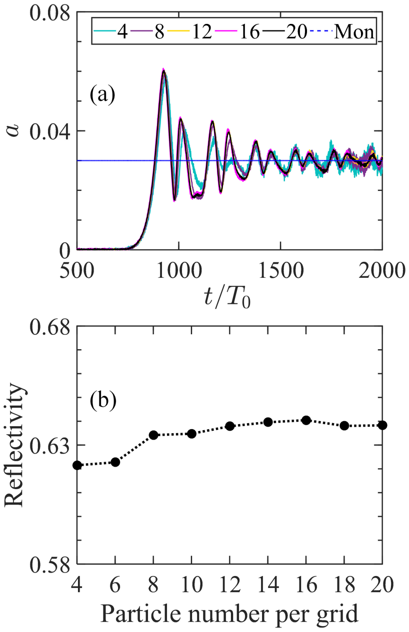

FIG. 6. (a) The intensity envelopes of the backscattered laser lights with different macro-particle numbers per grid varying from 4 to 20. The blue line titled 'Mon' (Monochromatic light) shows the intensity envelope of the incident laser light. (b) The reflectivity due to the LPIs with different macro-particle numbers per grid.

anti-Langmuir decay instability (ALDI), and Langmuir wave collapse near the quarter-critical density can cause the saturation of the backward SRS[54, 55]. In two-dimensional geometry, the two plasmon decay (TPD) instability that induces the efficient generation of hot electrons near the quarter-critical density will also compete with the SRS instability [12, 56].

VIII. NUMERICAL CONVERGENCE AND STABILITY

In the PM1D code, the electrons and ions are treated as macro-particles that are driven by the fluid forces. The number of macro-particles set in each grid may have some impacts on the simulation results. To get the dependence of the solution accuracy on the used macro-particle number, a series of simulations are carried out with the macro-particle number per grid varying from 4 to 20, while the laser vector potential $a_0 = 0.03$ and the plasma density $n_e = 0.4n_c$ remains constant. The simulation box has a total length of 300λ with 40λ vacuum in each side. A homogeneous plasma slab with a length of 220λ at the center of the simulation box with a 10λ density slope density slope in each side. The electron and ion initial temperatures are set as 1 keV and 100 eV, respectively. In the simulations, the grid size is set as 0.05λ and the time step is chosen as $0.0495T_0$. The particle number per grid is the only variable parameter in these simulations that varies from 4 to 20 evenly with a step of 2.

Figure 6(a) shows the intensity envelopes of the backscattered lights obtained from the PM1D simulations with different macro-particle numbers. It is demonstrated that the intensity envelopes of the backscattered lights in all cases have a similar evolution tendency. In particular, there are nearly no differences between the results if the macro-particle number per grid is larger than 8. Figure 6(b) shows the total reflectivity within $2000T_0$ due to the LPI with different particle numbers per grid. It is illustrated that the reflectivity quickly converges to about 0.637 with the increasing of the macro-particle number, and there is nearly no difference in the reflectivity if the macro-particle number per grid is larger than 8. It should be pointed out that the relative error of the reflectivity between the smallest particle number (4) and the maximum particle number (20) is only about 2.3%, which indicates that in the large scale simulations, a small particle number per cell can be adopted to save the simulation time and keep the expected accuracy of the solution simultaneously.

The LPIs in the ICF experiments generally develop in nanoseconds in time and several hundreds of microns in space. Therefore, the nonlinear simulation of the whole LPIs evolution will result in a huge computational cost and is unable to be performed by the typical kinetic codes like PIC or Vlasov even in one dimension. In the PM1D code, the particle number per grid can be greatly decreased comparing with the PIC codes while captures the kinetic effects simultaneously, which makes it possible to simulate large-scale long-time evolution of LPIs. In the long-time simulations of LPIs, however the numerical stability (the simulation results keep physical after a long time calculation) of the code becomes particularly important.

To verify the stability of the PM1D code, a test simulation is carried out for the time evolution of the SRS up to 200ps. In the simulation, a homogeneous plasma slab with a length of 300λ and density of $0.09n_c$ is adopted. The ions are assumed to be immobile and the initial electron temperature is 1 keV. The incident laser light has an intensity of 4.45×10^{15} W/cm^2 and a wavelength of 351 nm, the corresponding normalized vector potential is $a_0 = 0.02$. The time step $dt = 0.0495T_0$, the grid size $dx = 0.05\lambda$, and 4 macro-particles per grid are adopted in the PM1D code. For comparison, two PIC simulations are also carried out for the time evolution of the SRS up to 200ps, where the laser and plasma conditions keep the same as in the PM1D simulation and the grid size is $dx = 0.01$. In these two PIC simulations, 100 and 200 macro-particles are allocated per grid, respectively.

In Fig. 7(a), the spectrum of the backscattering SRS, the secondary scattering of SRS (the forward scattering of the primary backscattered light) as well as the anti-Stokes SRS can be identified in the long-time evolution of the backscattered light spectrum. More importantly,

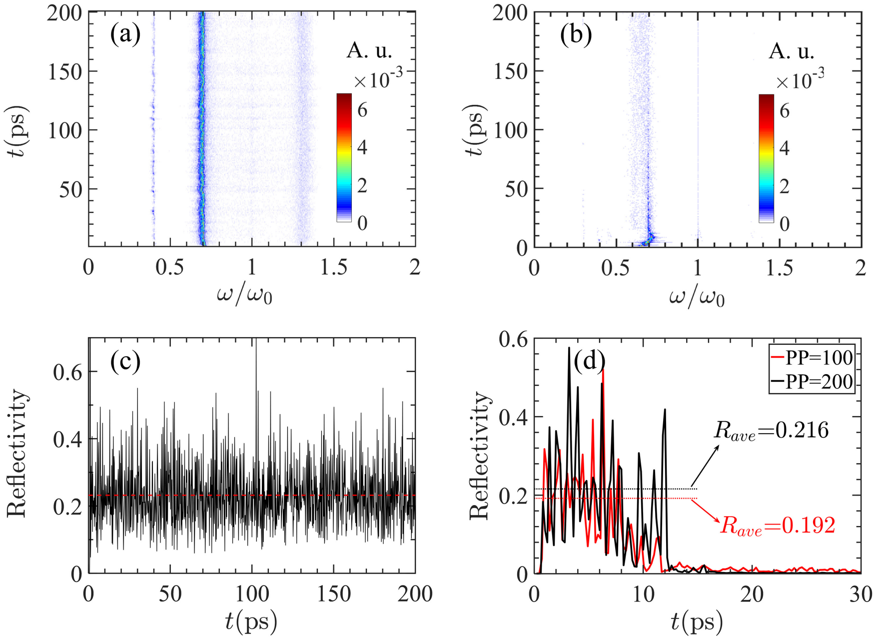

FIG. 7. (a) and (b) show the time evolution of the backscattering light spectrum in the evolution of the SRS up to 200ps calculated by the PM1D code and PIC code using 200 macro-particles per grid, respectively. (c)and (d) show the time evolution of the SRS reflectivity calculated by the PM1D code and PIC code (red line for 100 particles per grid and black line for 200 particles per grid), respectively.

the time evolution of the reflectivity of the SRS in Fig. 7(c) also illustrates a character of the bursting behavior of the SRS reflectivity. The average reflectivity within 200ps is about 23.2%. This simulation demonstrates the numerical stability of the PM1D code for the long-time evolution of the LPIs.

Figure 7(b) shows the spectrum of the backscattering SRS simulated by the EPOCH code using 200 macro-particles per grid, it can be found that the backscattering spectrum becomes very weak for $t \geq 10$ps, which is unreasonable in physics. From the time evolution of the SRS reflectivity displayed in Fig. 7(d), it is also confirmed that the SRS reflectivity drops sharply to zero after $t = 10$ps using either 200 or 100 macro-particles per grid. Here, we only show the SRS reflectivity before $t = 30$ ps since the reflectivity is almost zero after 30 ps. These simulation results indicate that the PIC code may not be suitable to simulate the long-time evolution of the SRS. Namely, the PIC code may not be numerically stable enough for the long time simulation of the SRS. The collapse of the PIC simulation might be due to the artificial electron heating in the long-time simulation process. Nevertheless, the averaged SRS reflectivity obtained from the PIC simulations within their reliable time are 0.192 and 0.216 for 100 and 200 macro-particles per grid, respectively. These two reflectivities are at the same level as the reflectivity obtained from the PM1D simulation. From Fig. 7(d), it is also found that the collapse of the PIC simulation can be slightly postponed by increasing macro-particle number per cell from 100 to 200. This implies that a huge macro-particle number may be helpful to the numerical stability of the PIC code.

Although the collapse of the PIC simulation might be caused essentially by the artificial electron heating, it is worth pointing out that the collapse time of the PIC simulation also depends on the boundary conditions as well as the laser-plasma parameters such as laser intensity. In the above PIC simulations, a finite homogeneous plasma with sharp plasma-vacuum interfaces is placed at the center of the simulation box, and the open boundary condition is adopted for the macro-particles at the boundary of the simulation box. The strong sheath fields near the plasma-vacuum interfaces in this case may drag back the hot electrons, therefore, some electrons will suffer the artificial heating several times. As a result, the collapse of the PIC simulation is speeded up. In another test simulation case using a semi-infinite homogeneous plasma with a thermal boundary condition, the energetic electrons that run away from the right boundary are replaced by the electrons with the initial temperature. By doing so, we find that the collapse of the PIC simulation can be postponed to about 20ps. We also note that the PIC simulation of LPIs can run steady for a longer time with a relatively low laser intensity [57, 58].

In contrast, the numerical heating in the PM1D code is relatively weak since the macro-particles are driven by the fluid force in the PM1D code rather than the Lorentz force. As a result, our PM1D code can operate steady at least up to 200 ps even using only 4 macro-particle per grid, which is crucial for decreasing the computational cost in the large-scale long-time simulations of the LPIs.

In Fig. 7, the long-time evolution of SRS is adopted to show the stability of the PM1D code, where the ions are assumed to be immobile. In the real cases, the ions are mobile, which will induce the SBS instability. When SBS and SRS are concomitant, the competition or interplay between these two instabilities may take place [59]. In particular, the backward scattering light of the absolute SRS at around $n_e = 0.2n_c$ may excite the SBS instability, which in turn becomes an important saturation mechanism of the backward SRS [57]. Further, the interplay between SRS and SBS can be utilized to weaken the total reflectivity of the pump laser light. For example, the total reflectivity can be decreased obviously if 2ω and 3ω lasers are incident together into the plasma under a special energy ratio, which provides a potential mechanism for the suppression of LPI in ICF [58].

IX. DISCUSSION AND SUMMARY

In summary, a PM1D code has been developed by using the particle-mesh method for the simulation of the SRS and SBS in laser-plasma interactions. Since the plasma is represented by freely-moving macro-particles in the PM method, this PM1D code can self-consistently simulate the breaking of plasma waves as well as other kinetic effects in the development of the LPIs. By designing a novel boundary condition that allows the incidence of the pump laser light and the emergence of the scattered light simultaneously, the incident and scattered laser lights can be described together in a single wave equation. This makes it convenient to get the complete form of the ponderomotive force in the electron motion equation, and hence the strongly nonlinear phenomena such as the density cavity formation can be treated suitably. The validity of the developed PM1D code is verified firstly by checking the linear growth rates for both the SRS and SBS, which quantitatively agree with the theoretical predictions. It is further verified by checking the nonlinear development of the LPIs by comparing them with standard PIC simulations. Just similar to PIC codes, this PM1D code can simulate the wave breaking, particle trapping, hot electron generation, and density cavity formation properly, all of which are challenges to the conventional fluid models. On the other hand, the computational cost with this PM1D code is obviously less than the typical PIC codes. More importantly, this PM1D code is very robust for the simulation of the long-time evolution of LPIs.

In the future work, we will also extend the PM1D code to the two-dimensional geometry. To this end, the electron momentum equation in Eq. (7) should be updated to take into account the two-plasmon decay instability. The 2D effects such as self-focusing and filamentation can be treated with the complete form of the ponderomotive force, which has already been included in Eq. (7). In the PM2D code, the laser propagation will also be described by the 2D wave equations. To study the CBET process, the incident laser beams with given transverse profiles should be allowed to be incident with certain angles and the scattered laser light should be absorbed on the boundary of the simulation box. It would be a critical issue to ensure the incident laser to be inputted and the scattered laser to be absorbed at the boundary simultaneously. The boundary condition we proposed in Eq.(19) and Eq.(20) will not be suitable for the 2D geometry at the oblique incidence cases. The perfectly matched layers (PML) may be an option for the boundary conditions.

ACKNOWLEDGMENTS

The work was supported by the Strategic Priority Research Program of Chinese Academy of Sciences (Grant No. XDA25050100), the National Natural Science Foundation of China (Grant Nos. 11975154, 11675108, 11655002, and 11775144) and Science Challenge Project (No.TZ2018005), and the China Scholarship Council. The work by ZMS has been carried out within the framework of the EURO fusion Consortium and has received funding from the European Union Horizon 2020 Research and Innovation Programme under Grant Agreement No. 633053. Simulations have been carried out on the Pi supercomputer at Shanghai Jiao Tong University.

---

[1] Kruer W 2019 *Physics of Laser Plasma Interactions* (CRC Press)
[2] Froula D H *et al* 2008 *Phys. Rev. Lett.* **101** 115002
[3] Montgomery D S 2016 *Phys. Plasmas* **23** 055601
[4] Craxton R S *et al* 2015 *Phys. Plasmas* **22** 110501
[5] Igumenshchev I V *et al* 2010 *Phys. Plasmas* **17** 122708
[6] Bergmann A and Mulse P 1993 *Phys. Rev. E* **47** 3585
[7] Glenzer S H, Rosmej F B, Lee R W, Back C A and Estabrook K G 1998 *Phys. Rev. Lett.* **81** 365
[8] Solodov A A *et al* 2020 *Phys. Plasmas* **27** 052706
[9] Simon A, Short R W, Williams E A and Dewandre T 1983 *Phys. Fluids* **26** 3107
[10] Seka W *et al* 2009 *Phys. Plasmas* **16** 052701
[11] Klimo O, Psikal J, Tikhonchuk V T, Weber S 2014 *Plasma Phys. Controlled Fusion* **56** 055010
[12] Xiao C Z *et al* 2015 *Phys. Plasmas* **22** 052121
[13] Weber S, Riconda C, Klimo O, Heron A and Tikhonchuk V T 2012 *Phys. Rev. E* **85** 016403
[14] Fernandez J C *et al* 2000 *Phys. Plasmas* **7** 3743
[15] Rousseaux C *et al* 2006 *Phys. Rev. Lett.* **97** 015001
[16] Michel D T *et al* 2013 *Phys. Plasmas* **20** 055703
[17] Maximov A V, Myatt J, Seka W, Short R W and Craxton R S 2004 *Phys. Plasmas* **11** 2994
[18] Rosenberg M J *et al* 2020 *Phys. Plasmas* **27** 042705

[19] Strozzi D J *et al* 2017 *Phys. Rev. lett.* **118** 025002
[20] Atzeni S *et al* 2005 *Comput. Phys. Commun.* **169** 153
[21] Yan R *et al* 2012 *Phys. Rev. Lett.* **108** 175002
[22] Weber S and Riconda C 2015 *High Power Laser Sci. Eng.* **3** e6
[23] Bertrand P and Ghizzo A 1990 *Phys. Fluids B* **2** 1028
[24] Banks J W, Berger R L, Brunner S, Cohen B I and Hittinger J A F 2011 *Phys. Plasmas* **18** 052102
[25] Chapman T, Berger R L and Cohen B I 2017 *Phys. Rev. Lett.* **119** 055002
[26] Strozzi D J, Shoucri M M and Bers A 2004 *Comput. Phys. Commun.* **164** 156
[27] Albritton J and Koch P 1975 *Phys. Fluids* **18** 1136
[28] Duda B J *et al* 1999 *Phys. Rev. Lett.* **83** 1978
[29] Froula D H, Divol L and Glenzer S H 2002 *Phys. Rev. Lett.* **88** 105003
[30] Vu H X, DuBois D F and Bezzerides B 2001 *Phys. Rev. Lett.* **86** 4306
[31] Neumayer P *et al* 2008 *Phys. Rev. Lett.* **100** 105001
[32] Yin L *et al* 2007 *Phys. Rev. Lett.* **99** 265004
[33] Karttunen S J and Salomaa R R E 1982 *Phys. Lett. A* **88** 350
[34] Heikkinen J A and Karttunen S J 1984 *Phys. Fluids* **27** 707
[35] Rozmus W, Casanova M, Pesme D, Heron A and Adam J C 1992 *Phys. Fluids B* **4** 576
[36] Weber S *et al* 2004 *Laser Part. Beams* **22** 189
[37] Ballereau Ph *et al* 2007 *Journal of Scientific Computing* **33** 1
[38] Divol L 2008 *Phys. Rev. lett.* **100** 255001
[39] Hu X Y 2015 *AIP Advances* **5** 087174
[40] Hüller S, Masson-Laborde P E, Pesme D, Casanova M, Detering F and Maximov A 2006 *Phys. Plasmas* **13** 022703
[41] Masson-Laborde P E, Hüller S, Pesme D, Casanova M, Loiseau P and Labaune Ch 2006 *J. Phys. IV France* **133** 247
[42] Myatt J F 2017 *Phys. Plasmas* **24** 056308
[43] Myatt J F 2019 *J. Comput. Phys.* **399** 108916
[44] Hao L, Yan R, Li J, Liu W D and Ren C 2017 *Phys. Plasmas* **24** 062709
[45] Lotekar A, Kakad A and Kakad B 2017 *Phys. Plasmas* **24** 102127
[46] Hockney R W and Eastwood J W 1988 *Simulation Using Particles* (CRC Press)
[47] Arber T D *et al* 2015 *Plasma Phys. Controlled Fusion* **57** 113001
[48] Dormand J R and Prince P J 1980 *J. Comp. Appl. Math.* **6** 19
[49] Engquist B and Majda A 1977 *Math. Comput.* **31** 139
[50] Brunner S and Valeo E J 2004 *Phys. Rev. Lett.* **93** 145003
[51] Lehmann G and Spatschek K H 2016 *Phys. Rev. Lett.* **116** 225002
[52] Winjum B J, Fahlen J and Mori W B 2007 *Phys. Plasmas* **14** 102104
[53] Yan R, Maximov A V, Ren C and Tsung F S 2009 *Phys. Rev. Lett.* **103** 175002
[54] Russell D A, DuBois D F and Rose H A 1999 *Phys. Plasmas* **6** 1294
[55] Feng Q S, Zheng C Y, Liu Z J *et al* 2018 *Phys. Plasmas* **25** 092112
[56] Stoeckl C, Bahr R E, Yaakobi B *et al* 2003 *Phys. Rev. Lett.* **90** 235002
[57] Feng Q S, Cao L H, Liu Z J *et al* 2020 *Scientific Reports* **10** 3492
[58] Feng Q S, Liu Z J, Cao L H *et al* 2020 *Nucl. Fusion* **60** 066012
[59] Walsh C J, Villeneuve D M, and Baldis H A 1984 *Phys. Rev. lett.* **53** 1445